19e Journées de l'Hydrodynamique
26 – 28 novembre 2024, Nantes

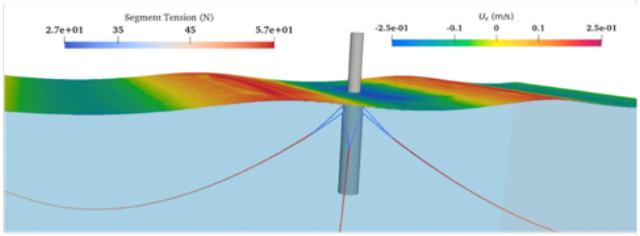

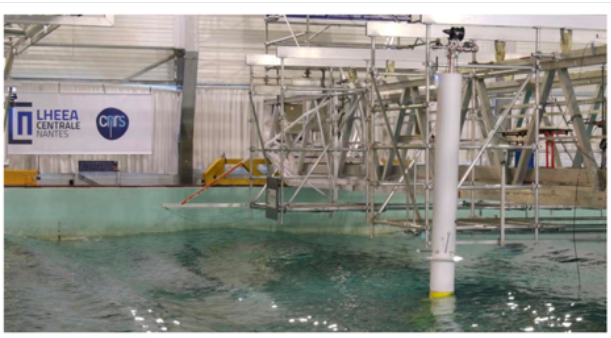

CHAMPS DE VAGUES INSTATIONNAIRES GENERES PAR UN NAVIRE S'AVANCANT DANS LA HOULE ET LEURS PROPRIETES SPATIO-TEMPORELLES

UNSTEADY WAVES GENERATED BY SHIPS ADVANCING IN REGULAR WAVES AND THEIR SPATIAL-TEMPORAL PROPERTIES

X.B. CHEN[1], Y. WANG[2], H. LIANG[3], G. DUCROZET[2]
xiao-bo.chen@bureauveritas.com

[1]Département de Recherche, Bureau Veritas M&O, Saint Herblain, France
[2]Nantes Université, École Centrale Nantes, CNRS, LHEEA, UMR 6598, Nantes, France
[3]Technical Centre for Offshore and Marine, Singapore (TCOMS), Singapore

Résumé

Le modèle HydroStar-V a été développé dans [7] pour évaluer les efforts exercés par la houle sur un navire avec vitesse d'avance, ainsi que les mouvements induits. Il se base sur la linéarisation de l'écoulement autour du navire par la méthode du double modèle et sur l'utilisation d'une fonction de Green avec effets visqueux. Les résultats du modèle sont en excellent accord avec les mesures expérimentales sur les coefficients de masse ajoutée et d'amortissement, les efforts d'excitation et les mouvements. Cette méthode a été récemment étendue au calcul de la résistance ajoutée et à l'évaluation des champs de vagues autour du navire.

Un navire animé d'une vitesse d'avance dans la houle crée à la fois un champ de vagues stationnaire et un champ de vagues instationnaire qui se superposent à la houle incidente. Le champ de vagues stationnaire (équivalent à celui généré par le navire en eau calme) a été analysé dans [11], et le champ instationnaire dans [6] pour la première fois, en utilisant la technique de la transformée de Fourier avec une fenêtre temporelle glissante. Les spectrogrammes obtenus fournissent des informations intéressantes sur les champs de vagues mesurés au point fixe. On a observé que ces champs de vagues ont des propriétés complexes mais fascinantes comme révélé dans [2]. Il a été notamment repéré des vagues d'amplitude importante qui déferlent autour du navire selon des lignes spécifiques qui se prolongent à une distance importante derrière le navire. Une méthode spécifique d'analyse de ces champs de vagues est proposée qui se base sur des transformées de Hilbert spatiales [16]. Elle permettra d'obtenir une représentation nombre-d'onde-fréquence du champ de vagues et d'analyser les vitesses de phase des crêtes de ce champ de vagues directionnel complexe.

Summary

The HydroStar-V method, based on the linearization over the ship-shaped stream (double-body flow) and the use of free-surface Green function with viscosity effects, has recently been developed in [7] to compute the wave loads on a ship advancing in waves and to evaluate the induced motions. Excellent agreement has been achieved between the numerical results and benchmark model tests concerning the added mass, radiation damping, wave excitation loads and ship motions. This method is recently extended to evaluate the second-order loads on ships, and to compute ship-generated steady and unsteady waves.

A ship advancing in regular waves generates both steady and unsteady ship waves in addition to the incoming waves. The steady ship waves (equivalent to those generated by ships in calm water) have been analyzed in [11], and unsteady ship waves in [6] for the first time, by using the technique of short-time Fourier transform. The obtained time-frequency spectrograms provide rich and useful information about these ship waves measured

at a fixed point. It is well observed that these ship-generated waves have complex but fascinating features as revealed in [2]. Notably, crests of large amplitude breaking along some lines in the vicinity of ship and continuously extending to some distance far behind the ship have been reported. A specific method, based on the spatial Hilbert transform [16], is applied to those ship-generated wave fields. This will allow a representation of the wave fields with *local* wavenumber-frequency maps, to compute and analyze the *local* crest phase speeds of this complex directional wave field.

I – Introduction

Considered as one of most difficult problems, the seakeeping prediction of a ship advancing in waves has been studied in many research and developments based on the potential theory and boundary integral method, including the simplified 2D strip theory, the 3D Rankine source method, and the free-surface Green function method, as summarized in [15]. Comparing these two mainstream 3D methods, i.e., one based on the use of free-surface Green function (GFM) and another based on the Rankine source method (RSM), the classical GFM reducing the number of unknowns is more advantageous than RSM, since the unknowns are located on the hull only thanks to the fact that the Green function satisfies the boundary condition on the free surface and the radiation condition which cause substantial difficulties in RSM. Furthermore, wavy properties (dispersive propagating waves) of potential flows are well represented by the Fourier elements in GFM while the Rankine source is fundamentally representative for local and non-wavy flows. One of fair examples concerns the zero-speed case. The great success of GFM in practical applications shows that GFM is incomparably superior to RSM, in terms of accuracy and efficiency. We have thus pursued this method in order to extend the success to the seakeeping with forward speed.

Indeed, our most recent results of research work on GFM are presented in [7]. The new method presented accumulates a series of critical groundwork in both theoretical and numerical aspects. On top of all, we have re-analysed the boundary value problem by choosing the ship-shaped stream as the base flow. This consideration is not only for physical acceptance but also necessary by a rigorous analysis based on the perturbation theory. The new and consistent boundary condition on the free surface is obtained with linearisation over the base flow. Unlike the usual boundary condition of Neumann-Kelvin type based on the uniform flow (physically unacceptable), the new formulation looks more complex due to interaction terms associated with the base flow.

We find the benefit of this complex boundary condition in the formulation of boundary integration equations. Green's third theorem is applied to the Green function and velocity potential of unsteady flow by performing the vector integral analysis of their respective differential equations. The part of free-surface integrand corresponding to the terms associated with the uniform flow is modified such that the equivalent waterline integral is proportional to the normal derivative of the base flow. This waterline integral is then simply nil by the boundary condition of base flow on ship hull. Free of waterline integral, it remains still integration of some free surface terms. This remaining integral over the free surface is localized in a limited zone as the integrand function depending on the ship-shaped stream is significant only in the vicinity of ship hull.

The Green function associated with a pulsating and translating source describes the fundamental solution to ship-motion problems with forward speed. Many studies have been carried out to analyse its behaviours and to develop numerical schemes for its computations. The most striking property is the peculiar singularity and fast oscillations for field points approaching to the track of source point at or close to the free surface, as revealed in [8]. This behaviour makes the waterline integral included in the classical BIE (Classical NK) nightmarish. The same issue should be encountered in the computation of the free-surface integral involved in the New BIE.

Not satisfied with using treatments by lowering the waterline or by parametrising numerical filters to mask the difficulty, we have examined its origin by introducing the neglected physical parameters like surface tension, fluid viscosity or both. We have chosen the introduction of viscosity. Unlike the classical way introducing fictitious viscosity (Rayleigh viscosity or Lighthill's argument) which was just a mathematical device to make waves propagating radially outwards, the analysis based on linearised Navier-Stokes equation and Helmholtz decomposition in [4] yields the consistent kinematic and dynamic boundary conditions on the free surface with viscosity.

The Green function with viscosity is then adopted. Unlike the inviscid Green function, there are three wavenumbers all of which are complex. First two wavenumbers look like those of inviscid Green function for small and moderate values, but significantly different for θ close to $\pi/2$. They can be large but not unbounded and have an important imaginary part which damps all highly oscillatory waves. The third one having a negative real part does not generate any waves and contribute to the local field. Being implicit and complex, the integrand function of viscous Green function is free of singularities and numerical computations are facilitated.

As the matrix elements of linear system, the influence coefficients are the integration of Green function and its derivatives on ship hull H and on free surface F. To guarantee the accuracy, analytical integrations of the wavenumber integral function and its derivatives over flat panels of polygonal form are formulated for

all configurations including panels of hull-to-hull, hull-to-freesurface and freesurface-to-freesurface. The usual algorithm using Gauss points gives good accuracy for integration on hull panels. It is, however, necessary to use excessive number of Gauss points to obtain a correct accuracy for panels on the free-surface.

To take advantages associated with the accuracy in the analytical integrations of Green function over flat panels, we adopt the concept to use flat panels inside a bi-quadratic curved patch represented by using shape functions. The velocity potential obtained by New BIE (Present GFM) on flat panels can be accurately extended to its tangent derivatives necessary for pressure computations, by the derivatives of the shape functions.

To be sure that Green's third theorem is well respected outside the fluid domain, the zero potential on the waterplane inside the ship hull is imposed in addition to BIEs on the hull and on the free surface. This over-determined linear system method, described in [12], has been successful to remove the effect of "irregular frequencies", in our in-house software HydroStar for the solution of seakeeping at zero speed. Application of this approach guarantees the well-conditioning of linear system. Indeed, there is an issue of "irregular wavenumbers" associated with BIEs in the forward-speed problem. As mentioned in [7], similar to the zero-speed case which is a special case of forward-speed problems, the effect of "irregular wavenumbers" appears for every encounter frequency, remarkable by exaggerated oscillations of elementary solutions, in particular, the damping coefficients obtained by using the Classical NK method. In the present GFM, smooth variation of added-mass and damping coefficients illustrated in [7] demonstrates the efficiency of the approach used to remove the effect of irregular wavenumbers.

The consistent decomposition of radiation coefficients and inclusion of speed-effect restoring forces are critically important. Indeed, the extraction of restoring forces embedded in the classical definition of added-mass coefficients yields finite values for all coefficients at low-frequency range. The finding of restoring forces due to the steady-flow pressure clarifies the controversy of non-zero stiffness in the horizontal directions and keeps the physical consistency. Ship motions associated with the effect of restoring forces due to forward speed are predicted with much improved accuracy.

Careful implementation of the present GFM has been realised in our in-house software HydroStar-V . Numerical results obtained by using HydroStar-V are validated with classical benchmark cases, in particular, the Wigley IV hull with a length-to-width ratio = 5 for which the effect of steady flow is important. The first comparison has received many interesting discussions. The most recent experimental measurements on RIOS bulk carrier summarized in [17], have been used to compare numerical results. In all cases, very good agreement is obtained.

It is well observed that these ship-generated waves have complex but fascinating features as revealed in [2]. Notably, crests of large amplitude breaking along some lines in the vicinity of ship and continuously extending to some distance far behind the ship have been reported. Here, we present our analysis on unsteady ship waves by using the technique of short-time Fourier transform, further to that in [6]. The obtained time-frequency spectrograms provide rich and useful information about these ship waves measured at a fixed point. Furthermore, a specific method, based on the spatial Hilbert transform [16], is also applied to those ship-generated wave fields. These will allow a representation of the wave fields with local wavenumber-frequency maps and to compute the local crest phase speeds of this complex directional wave field. Once the phase speed is determined and associated with fluid velocity, it is possible to detect the ship wave breaking event through the so-called kinematic breaking threshold, i.e. the ratio of fluid velocity and phase speed.

II – Time-harmonic flows in HydroStar-V method

We define a Cartesian coordinate system $(O-XYZ)$ fixed on the earth by choosing its (X,Y) plane to coincide with the undisturbed free surface and the $Z-$axis oriented positively upward, and a moving coordinate system $(o-xyz)$ in parallel with $(O-XYZ)$ but to move at the same constant speed as ship along the positive x direction. The relationship between these two coordinate systems is given by

$$\begin{aligned} x &= X + X_0 - U(T - T_0) \\ y &= Y + Y_0 \\ z &= Z \end{aligned} \tag{1}$$

in which (X_0, Y_0) are the coordinates of the origin o at the instant T_0. The constants (X_0, Y_0, T_0) are usually put to be zero or $X_0 = -UT_0$ & $Y_0 = 0$, for the sake of simplicity.

In the moving coordinate system translating at the speed $F_{\rm r} = U/\sqrt{gL}$ scaled with the acceleration due to gravity g and ship length L, the fluid motion is represented by the velocity potential

$$\Psi(x,y,z,t) = U\big[\bar{\phi}_0(x,y,z) - x\big] + \bar{\phi}_w(x,y,z) + \varphi(x,y,z,t) \tag{2}$$

in which $\bar{\phi}_0(x,y,z)$ the ship-shaped stream, the wavy steady potential $\bar{\phi}_w(x,y,z)$ and the time-harmonic velocity potential $\varphi(x,y,z,t)$. The time-harmonic potential is further written by

$$\varphi(x,y,z,t) = \Re\mathrm{e}\left\{\phi(x,y,z)\mathrm{e}^{-\mathrm{i}\omega t}\right\} \tag{3}$$

with the scaled frequency $\omega = \omega_e\sqrt{L/g}$ and $t = T\sqrt{g/L}$. The ship-shaped stream $\bar{\phi}$ satisfies the boundary condition on the mean surface F and on the ship hull H

$$\begin{aligned} \partial_z\bar{\phi}_0 &= 0 \qquad F \\ \partial_n\bar{\phi}_0 &= n_1 \qquad H \end{aligned} \tag{4}$$

respectively, with n_1 the x-component of the normal vector $\mathbf{n} = (n_1, n_2, n_3)$ defined on H positively towards interior of the fluid. The gradient of ship-shaped stream being denoted by $\mathbf{w} = \nabla(\bar{\phi}_0 - x) = \nabla\bar{\phi}_0 - \mathbf{i}$, the linearized boundary condition on the mean free surface

$$\partial_z\phi - \omega^2\phi - 2\mathrm{i}\tau\mathbf{w}\cdot\nabla\phi + F_\mathrm{r}^2\mathbf{w}\cdot\nabla(\mathbf{w}\cdot\nabla\phi) + F_\mathrm{r}^2\nabla\phi\cdot(\mathbf{w}\cdot\nabla)\mathbf{w} + \partial_{zz}\bar{\phi}_0(\mathrm{i}\tau\phi - F_\mathrm{r}^2\mathbf{w}\cdot\nabla\phi) = 0 \tag{5}$$

with the Brard number $\tau = \omega F_\mathrm{r}$, satisfied by the unsteady potential on F. The boundary condition on the ship hull is written on H at its mean position

$$\partial_n\phi = \begin{cases} -\xi_0\partial_n\phi_0 & \text{diffraction} \\ \xi_j(-\mathrm{i}\omega n_j + F_\mathrm{r}m_j) & \text{radiations} \end{cases} \tag{6}$$

The potential ϕ_0 representing incoming waves is known to take Airy's form

$$\phi_0 = -\mathrm{e}^{k_0 z + \mathrm{i}k_0(x\cos\beta + y\sin\beta)}/\omega_0 \tag{7}$$

with the wave frequency ω_0 scaled with $\sqrt{L/g}$, the wavenumber $k_0 = \omega_0^2$ and wave heading β. In (11), ξ_0 is the amplitude of incoming waves and ξ_j for $j = 1, 2, \cdots, 6$ denote the six elementary motions including the translations $\mathbf{T} = (\xi_1, \xi_2, \xi_3)$ and rotations $\mathbf{R} = (\xi_4, \xi_5, \xi_6)$ around the centre of gravity. The vector components (n_j, m_j) for $j = 1, 2, \cdots, 6$ are those of the generalized normal vector and those of m_j terms depending on ship-shaped stream $\mathbf{w}$, given in [14] :

$$\begin{aligned} (n_1, n_2, n_3) &= \mathbf{n} \\ (n_4, n_5, n_6) &= \mathbf{r}\wedge\mathbf{n} \\ (m_1, m_2, m_3) &= -(\mathbf{n}\cdot\nabla)\mathbf{w} \\ (m_4, m_5, m_6) &= -(\mathbf{n}\cdot\nabla)(\mathbf{r}\wedge\mathbf{w}) \end{aligned} \tag{8}$$

with the position vector $\mathbf{r}$ defined by

$$\mathbf{r} = \{x - x_G, y - y_G, z - z_G\} \tag{9}$$

with respect to the center of gravity $\mathbf{r}_G = (x_G, y_G, z_G)$. Following the boundary condition (11) on H, the unsteady potential can be decomposed by

$$\phi = \sum_{j=1}^{6}\xi_j(-\mathrm{i}\omega\phi_j + F_\mathrm{r}\phi_{j+6}) + \xi_0\phi_{13} \tag{10}$$

associated with the boundary condition

$$\partial_n\phi_j = \begin{cases} n_j & j = 1, 2, \cdots, 6 \\ m_{j-6} & j = 7, 8, \cdots, 12 \\ -\partial_n\phi_0 & j = 13 \end{cases} \tag{11}$$

on H. It is worth noting that the boundary condition (5) should be satisfied by ϕ_j for $j = 1, 2, \cdots, 12$ individually, and by the sum $\phi_{13} + \phi_0$ of diffraction potential ϕ_{13} and that of incoming waves ϕ_0 given by (7) so that (5) becomes non-homogeneous (a non-zero forcing term) associated with ϕ_0 for diffraction problem.

Applying the Green's theorem to the couple functions (ϕ_j, G) in the fluid domain, the velocity potential $\phi_j(P)$ for $j = 1, 2, \cdots, 13$ can be expressed by the surface integral

$$\begin{aligned} \phi_j(P) = &\iint_H \left[\partial_n\phi_j(Q)G(P,Q) - \phi_j(Q)\partial_n G(P,Q)\right]\mathrm{d}S(Q) \\ &+ \iint_F \left[F_0(P,Q)\phi_j(Q) + F_1(P,Q)\partial_x\phi_j(Q) + F_2(P,Q)\partial_y\phi_j(Q)\right]\mathrm{d}S(Q) \end{aligned} \tag{12}$$

involving $G(P,Q)$ the Green function, and $F_{0,1,2}(P,Q)$) are dependent on the ship-shaped stream $\bar{\phi}(Q)-x$, and $G(P,Q)$, given in [7], which are only significant in the vicinity of ship hull. Applying (12) for a field point $P(\xi,\eta,\zeta)$ on the hull H, the new BIE is then written as

$$\frac{1}{2}\phi_j(P)+\iint\limits_H \phi_j\partial_n G\,\mathrm{d}S-\iint\limits_F (F_0\phi_j+F_1\partial_x\phi_j+F_2\partial_y\phi_j)\,\mathrm{d}S=\iint\limits_H G\partial_n\phi_j\,\mathrm{d}S \tag{13}$$

for $P\in H$, which should be combined with one BIE on the free surface since (ϕ,ϕ_x,ϕ_y) are unknown on F. Similar to the new BIE on H, the BIE for a field point P on the free surface is obtained

$$\phi_j(P)+\iint\limits_H \phi_j\partial_n G\,\mathrm{d}S-\iint\limits_F (F_0\phi_j+F_1\partial_x\phi_j+F_2\partial_y\phi_j)\,\mathrm{d}S=\iint\limits_H G\partial_n\phi_j\,\mathrm{d}S \tag{14}$$

for $P(\xi,\eta,\zeta=0)\in F$. In addition, we apply the third Green theorem to a field point P located inside the ship, i.e., outside of the fluid domain limited by $H\cup F$. In particular, at some points on the waterplane denoted by W, the integral equation is written as

$$\iint\limits_H \phi_j\partial_n G\,\mathrm{d}S-\iint\limits_F (F_0\phi_j+F_1\partial_x\phi_j+F_2\partial_y\phi_j)\,\mathrm{d}S=\iint\limits_H G\partial_n\phi_j\,\mathrm{d}S \tag{15}$$

for $P(\xi,\eta,\zeta=0)\in W$ inside the ship hull.

The hull integral on the left hand side of (13) and the free-surface integral of (14) represent the principal value in the sense of Cauchy. As mentioned foregoing, there is, in addition, an integral on F on the right hand side of (13)-(15) associated with the forcing term due to incoming waves (7) for the diffraction problem, is given explicitly in [7]. The linear system combining BIE on H (13) and BIE on F (14) is of square form, i.e., the same number of equations as that of unknowns, since the tangent derivatives of unknowns on F can be transformed to unknowns ϕ by using shape functions in higher-order patch method, or any scheme of finite-difference type. In order to be sure that Green's third theorem is well respected outside of the fluid domain - zero potential inside the ship. The additional equation (15) is formulated for P on the waterplane W. The system is then over-determined. A linear system of rectangular form can be resolved using the standard Lapack library.

The Green function $G(P,Q)$ involved in (13)-(15) is the space function in the definition

$$\mathcal{G}(x,y,z,t)=\Re\mathrm{e}\left\{G(x,y,z)\mathrm{e}^{-\mathrm{i}\omega t}\right\} \tag{16}$$

representing the fundamental solution at the field point $P(\xi,\eta,\zeta)$ associated with a translating and pulsating source located at $Q(x,y,z)$. It satisfies the special Poisson equation

$$\nabla^2 G(P,Q)=4\pi\delta(|P-Q|) \tag{17}$$

with $\delta(\cdot)$ the Dirac delta function, in the fluid domain. Based on the thorough analysis of the Laplace-Fourier transform applied to the Stokes flow, in [3], the leading effect of vorticity is represented by an additional term appearing in the boundary condition at the free surface. Indeed, the linear boundary condition with dissipation is written by

$$G_z-\omega^2 G-2\mathrm{i}\tau G_x+F_\mathrm{r}^2 G_{xx}-4\bar{\epsilon}(F_\mathrm{r}G_{xzz}+\mathrm{i}\omega G_{zz})=0 \tag{18}$$

on $z=0$. In (18), the coefficient $\bar{\epsilon}=\nu/\sqrt{gL^3}$ is proportional to the fluid kinematic viscosity ν. It is shown that the magnitude of elementary waves $\mathrm{e}^{k\zeta+\mathrm{i}(k\xi-\omega t)}$ decays like $\mathrm{e}^{-4\epsilon\omega k^2|\xi|}$ and more rapidly with short waves of large wavenumber. This implies that the complex singular and highly oscillatory behaviours in $G(P,Q)$ due to short waves predicted in [8] just disappear.

By applying Fourier transform to differential equations satisfied by the Green function, we write

$$G(P,Q)=-1/r+1/r'+G^F(P,Q) \tag{19}$$

in which $r=|P-Q|$ is the distance between the source point $Q(x,y,z)$ and the field point $P(\xi,\eta,\zeta)$ and $r'=|P-Q'|$ is that between the mirror source $Q'(x,y,-z)$ and $P(\xi,\eta,\zeta)$. The free-surface term $G^F(P,Q)$ is given by the Fourier integral in polar (k,θ) coordinates

$$F_\mathrm{r}^2 G^F(P,Q)=\frac{1}{\pi}\int_{-\pi}^{\pi}\mathrm{d}\theta\int_0^\infty \mathrm{d}k\,\frac{k}{D(k,\theta)}\mathrm{e}^{kZ} \tag{20}$$

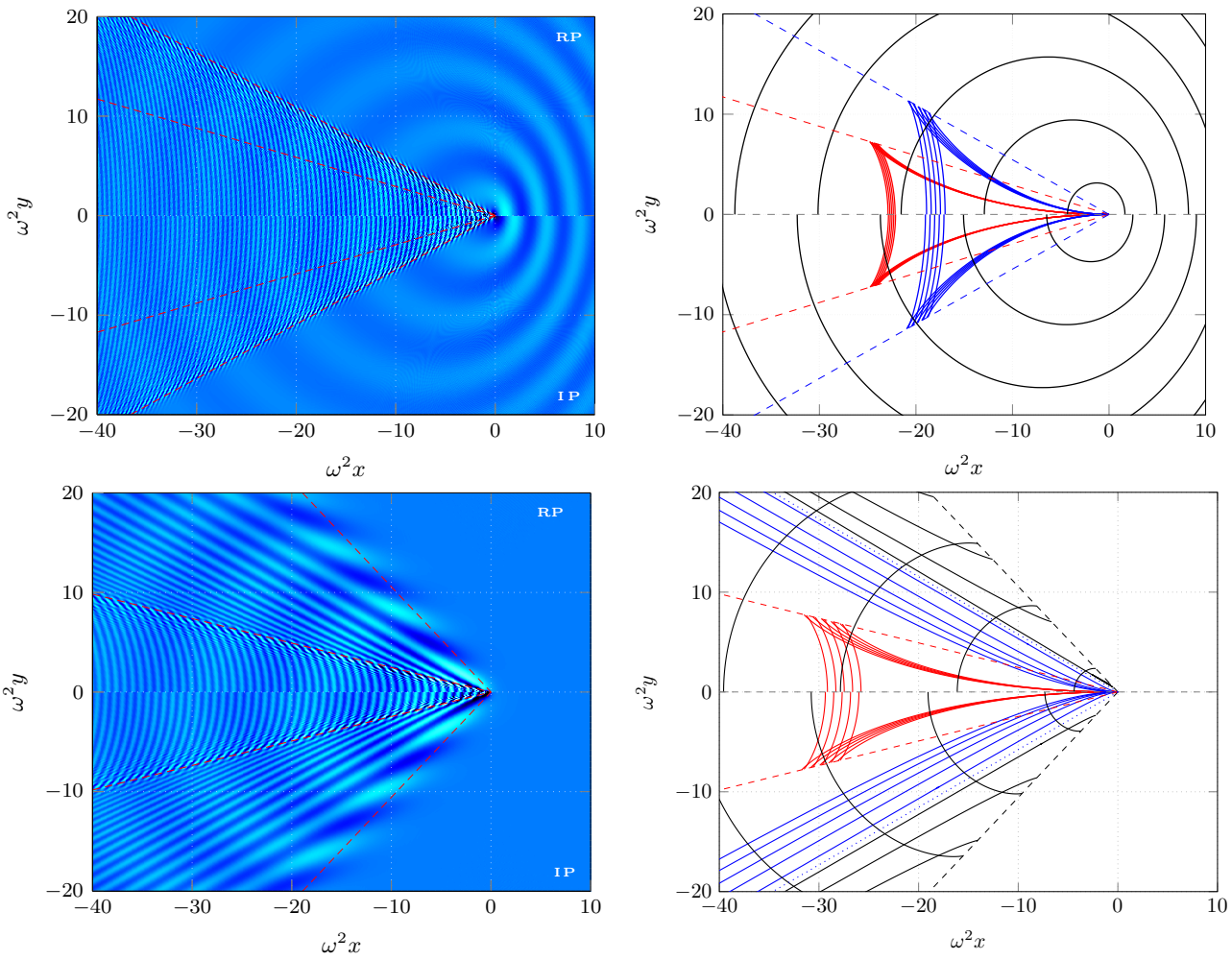

FIGURE 1 – Wave patterns (left) and crestlines (right) for $\tau = 0.2$ (top) and $\tau = 0.5$ (bottom)

with the speed-scaled Fourier variable k and $Z = \mathrm{v} - \mathrm{i}\mathrm{w}$ with

$$\begin{aligned} \mathrm{v} &= (\zeta + z)/F_\mathrm{r}^2 \leqslant 0 \\ \mathrm{w} &= \cos\theta(\xi - x)/F_\mathrm{r}^2 + \sin\theta(\eta - y)/F_\mathrm{r}^2 \end{aligned} \tag{21}$$

in their speed-scaled form. The denominator of the integrand function in (20) is the dispersion function resultant from the Fourier transform of the boundary condition (18) in [4] written by :

$$D(k,\theta) = (k\cos\theta - \tau)^2 - k - \mathrm{i}4\epsilon(k\cos\theta - \tau)k^2 \tag{22}$$

The coefficient ϵ in (22) is scaled by $\epsilon = \nu/(F_\mathrm{r}^3\sqrt{gL^3}) = \nu g/U^3$. The cubic dispersion equation $D(k,\theta) = 0$ gives three complex roots denoted by :

$$k_{1,2,3}(\theta) = \kappa_{1,2,3}(\theta) + \mathrm{i}\mu_{1,2,3}(\theta) \tag{23}$$

which can be found by applying Cardano's formulae. Once we have the wavenumbers k_i for $i = 1, 2, 3$ (roots of dispersion equation), the inner integral in k can be performed analytically so that

$$F_\mathrm{r}^2 G^F(P,Q) = \frac{1}{\pi}\int_{-\pi}^{\pi}\Big[A_1 K(Z,k_1) + A_2 K(Z,k_2) + A_3 K(Z,k_3)\Big]\,\mathrm{d}\theta \tag{24}$$

called formulation of Havelock type, in which $K(Z,k_i)$ is called wavenumber integral function given in [3] as

$$K(Z,k_i) = \int_0^\infty \frac{\mathrm{e}^{kZ}}{k-k_i}\,\mathrm{d}k = \mathrm{e}^{k_i Z}E_1(k_i Z) + \mathrm{i}\pi\left[\mathrm{sgn}(\mu_i) + \mathrm{sgn}(\mu_i \mathrm{v} - \kappa_i \mathrm{w})\right]H(\kappa_i)\mathrm{e}^{k_i Z} \tag{25}$$

with the sign function $\mathrm{sgn}(\cdot)$, the Heaviside function $H(\cdot)$ and the exponential-integral function $E_1(\cdot)$ defined by (eq.5.1.1) in [1]. The amplitude functions $A_i(\theta)$ for $i = 1, 2, 3$ in (24) are of regular function which can have

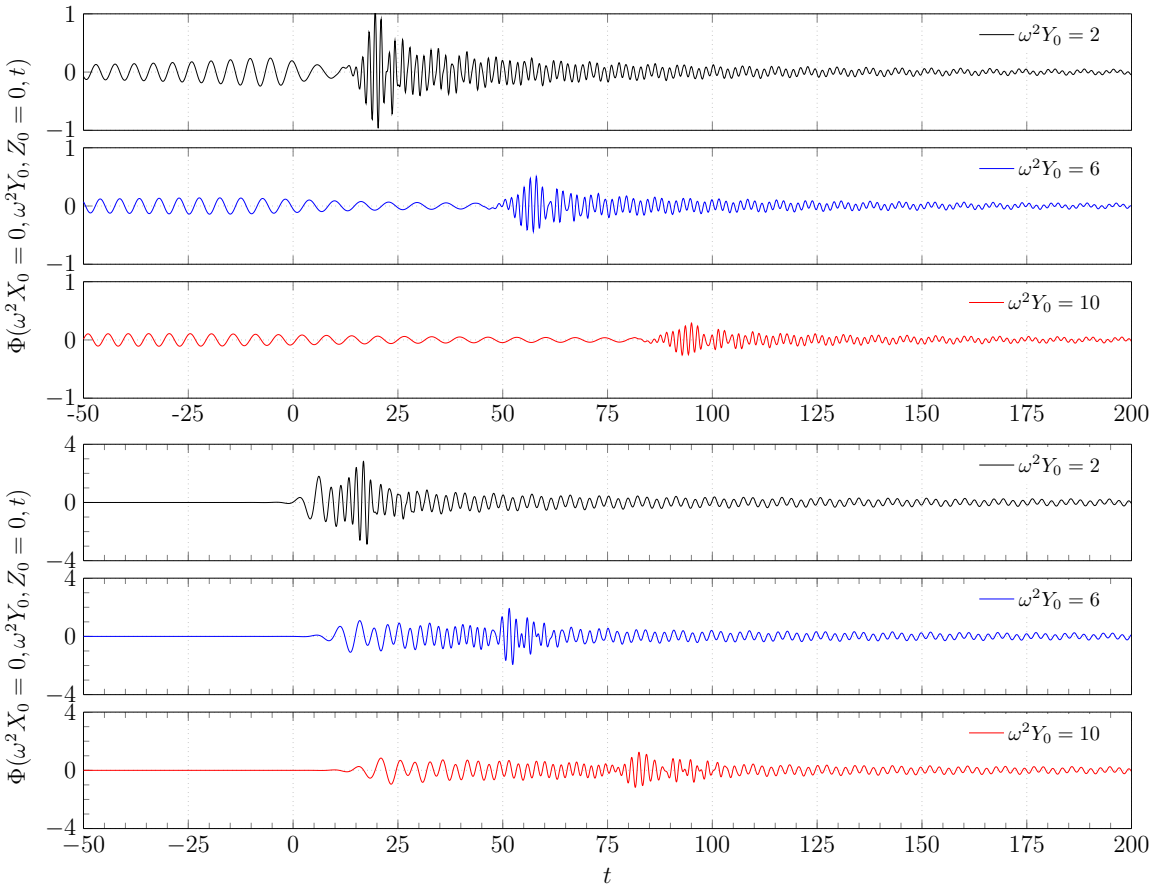

FIGURE 2 – Time series of time-harmonic ship waves for $\tau = 0.2$ (top) and $\tau = 0.5$ (bottom) at $\omega^2 X_0 = 0$ and $\omega^2 Y_0 = 2$ (first line), 6 (second line) and 10 (third line)

sharp variation at $\theta = \pm(\pi - \theta_c)$ with $\theta_c = \arctan(16\tau^2 - 1)$ for $\tau > 1/4$. Furthermore, the wavenumber integral function $K(Z, k_i) = K(P, Q, \theta, k_i) = K(a_i + \mathrm{i}b_i)$ with (a_i, b_i) being real numbers depending on $(\kappa_i, \mu_i, \mathrm{v}, \mathrm{w})$ according to its definition (25) is a regular function for $\mathrm{v} < 0$, except for a logarithmic singularity at $\mathrm{v} = 0 = \mathrm{w}$.

The integration of $K(Z, k_i)$ over a flat panel is formulated analytically by using the node coordinates of the panel. The efficient formulation is developed by inspiring from the course handout [9] and by applying Stokes' theorem to transform a panel surface integral to a contour integral along the panel's sides.

III – Kinematics of time-harmonic ship waves

The analysis of the wavenumber integral function defined by (25) shows that the first term on the right hand side is a smooth and non-oscillatory function. The second term is of oscillatory and determines the wave component associated with the point source. There are three wavenumbers (23) by the dispersion equation of which the third one has a negative real part ($\kappa_3 < 0$) so that it does not contribute to the wave component. The polar integral (24) associated with the first two wavenumbers can be, in fact, converted to simple line integral along associated wavenumber curves in the Fourier plane. Indeed, the analysis in [2] based on the method of stationary phase, gives the direct relationship between the geometrical properties of dispersion curves in the Fourier plane and the characteristics of far-field waves including crestlines of different wave systems with their wavelength and cusp angles, phase and group velocities, etc.

The wave patterns associated with a point source located at the origin obtained by (24) are depicted on the left part of Figure 1 for $\tau = 0.2$ on the top and $\tau = 0.5$ on the bottom. In each picture with color map, the real part and imaginary part are drawn on the upper half and lower half, respectively. On the other side, the crestlines associated with a series of constant phases are depicted on the top-right of Figure 1 for $\tau = 0.2$ and those on the top-right of Figure 1 for $\tau = 0.5$, respectively. Three distinct wave systems are remarkable for $\tau = 0.2$. The ring wave system with shorter and longer wavelengths on upstream and downstream, respectively, in accordance with the Doppler effect. The two other systems of V-shape waves are inner-V and outer-V waves with smaller and larger cusp angles, respectively. The ratio between wavelengths of V waves and ring waves is

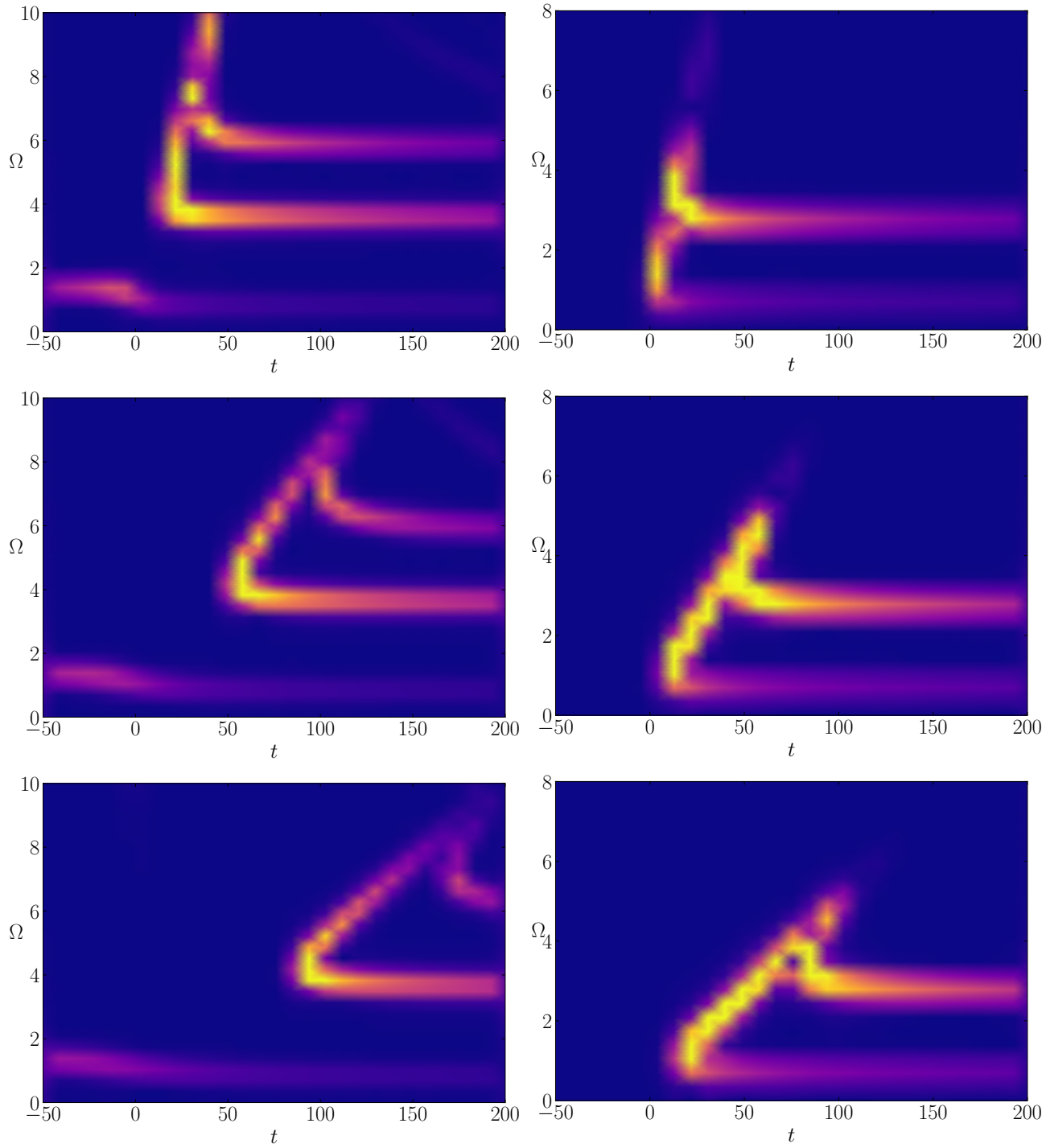

FIGURE 3 – Time-frequency spectrograms of time series for $X_0 = 0$ and $\omega^2 Y_0$=2 (top), 6 (middle) and 10 (bottom) at $\tau = 0.2$ (left column) and $\tau = 0.5$ (right column)

proportional to $\tau^2 = 0.04$ so that V waves are of very short wavelength. In Figure 1 showing wave patterns at $\tau = 0.5$, inner-V waves with smaller cusp angle and ring-fan waves with larger cusp angle. Both wave systems are present only on the downstream.

In the moving coordinate system, the time-harmonic waves are of a unique frequency as defined in (3) and (16). In the earth-fixed coordinate system, they can be expressed by

$$\begin{aligned} \varphi(X,Y,Z,t) &= \Re\mathrm{e}\left\{\phi(X-F_{\mathrm{r}}t,Y,Z)\mathrm{e}^{-\mathrm{i}\omega t}\right\} = \Re\mathrm{e}\left\{\Phi(X,Y,Z)\mathrm{e}^{-\mathrm{i}\Omega t}\right\} \\ \mathcal{G}(X,Y,Z,t) &= \Re\mathrm{e}\left\{G(X-F_{\mathrm{r}}t,Y,Z)\mathrm{e}^{-\mathrm{i}\omega t}\right\} = \Re\mathrm{e}\left\{\tilde{G}(X,Y,Z)\mathrm{e}^{-\mathrm{i}\Omega t}\right\} \end{aligned} \tag{26}$$

with the frequency Ω dependent on the position (X, Y) of observer on the earth.

The time series (26) measured at a fixed point (X_0, Y_0) are depicted in Figure 2 for $\tau = 0.2$ on the top with $X_0 = 0$ and $\omega^2 Y_0 = 2$ by the first line, 6 (second line) and 10 (third line), and for $\tau = 0.5$ on the bottom, with $\omega^2 X_0 = 0$ and $\omega^2 Y_0 = 2, 6$ and 10, respectively. At $\tau = 0.2$, ring waves are present for $t < 0$, i.e., at a position $x > 0$ on the upstream. The oscillation frequency is higher than the encounter frequency on the upstream and much lower on the downstream. The superposition of three wave systems (inner-V, outer-V and ring waves) yields a quite complicated time series. At $\tau = 0.5$, no waves on the upstream when $t < 0$. Only waves are present for $t > 0$, i.e., on the downstream ($x < 0$) where the inner-V waves and ring-fan waves are superposed.

The method based on the short-time FFT to obtain time-frequency spectrograms (TFS) and developed in [10, 11] is applied to analyze these time series. The TFS "heat" maps for $\tau = 0.2$ with $\omega^2 Y_0 = 2, 6$ and 10 corresponding to the three time series in Figure 2 are illustrated on the left column of Figure 3. It is remarkable to see some strips (bands) of *L-shaped boomerangs* with two wings (branches). Unlike steady ship waves whose TFS present only one L-shaped boomerang with a horizontal branch (transverse waves) and a slanting one (divergent waves), here we have two boomerangs and one additional band at very low frequencies. The two L-shaped boomerangs are associated with the inner-V waves on the top and the outer-V waves at a lower position, respectively. The horizontal branches correspond to transverse waves in the inner-V and outer-V wave systems, while the slanting branches correspond to divergent waves. The two branches of outer-V waves are joined together at $t \approx 18$, 54 and 96 while those of inner waves at $t \approx 34$, 102 and 170, respectively. The low-frequency bands on the bottom of heat maps are associated with ring wave system and present for both $t < 0$ (upstream) and $t > 0$ (downstream). The frequency is higher for $t < 0$ and much lower for $t > 0$.

At $\tau = 0.5$, there exist again two L-shaped boomerangs illustrated in Figure 3. The one on the top is associated with the inner-V waves and another on the bottom with ring-fan waves. The horizontal branch of lower boomerang is at very low frequency corresponding to partial ring waves and the slanting branch with increasing frequency linked to the fan waves. The upper boomerang is similar to the top one at $\tau = 0.2$ as it is associated with the inner-V wave system. The two branches of ring-fan waves join at $t \approx 3.8$, 11 and 19 for $\omega^2 Y_0 = 2$, 6 and 10, respectively.

It is important to note mistakes in the Figures 3-4 and Figures 5-6 presented in [5], which are corrected and reprinted here as Figure 2 for the time series and Figure 3 for the time-frequency spectrograms, respectively. More information like the slope of slanting branches, and nodes where spectrum values are minimum along the slanting branches of divergent waves and fan waves, as well as those along the partial-ring waves, which can

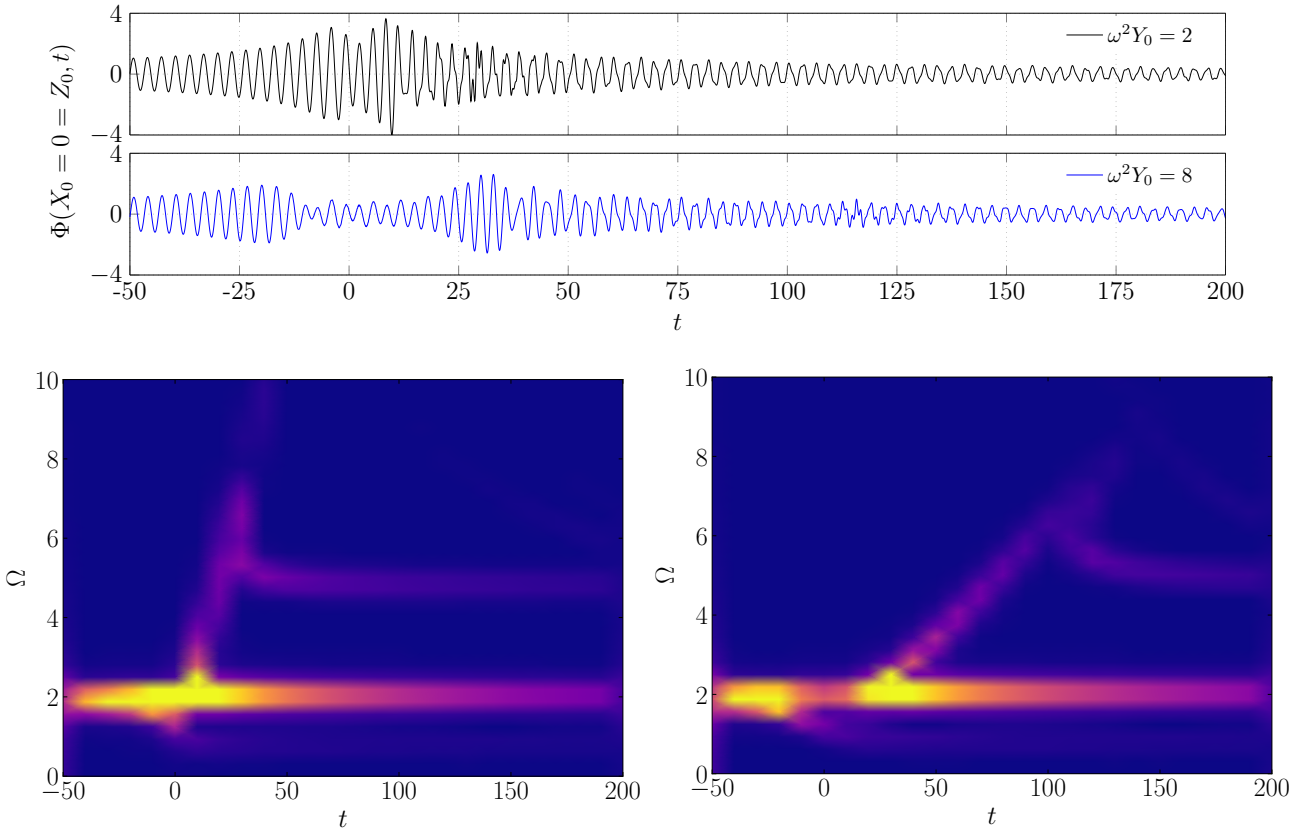

FIGURE 4 – Time series of time-harmonic ship waves (top) for $\tau = 0.2499$ at $\omega^2 X_0 = 0$ and $\omega^2 Y_0 = 2$ (first line) and 8 (second line), and its TFS (bottom) at $\omega^2 X_0 = 0$ and $\omega^2 Y_0 = 2$ (left) and 8 (right)

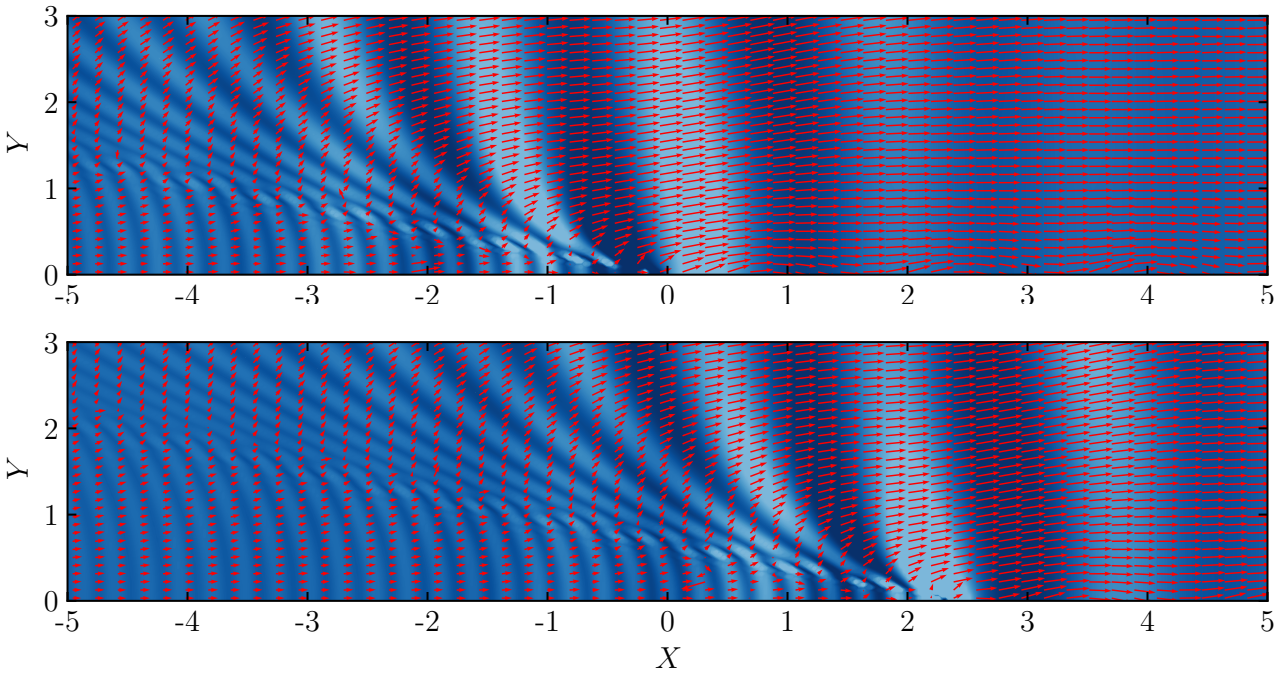

FIGURE 5 – Phase velocity vectors of unsteady ship waves in the earth-fixed coordinate system for $\omega = 1$ and $F_{\mathrm{r}} = 0.251$ at $t = 0$ on the upper part and $t = 10$ on the lower part

be derived in a way similar to that used in [10, 11], is also insightful for understanding physical properties of unsteady ship waves.

At a special case of $\tau = 0.2499$ with ($\omega = 1$ and $F_{\mathrm{r}} = 0.2499$), the times series generated by a point source at $(X_0, Y_0) = (0, 2)$ and $(X_0, Y_0) = (0, 8)$ are depicted by the first line and second line, respectively, on the upper part of Figure 4. Waves are present in both upstream ($t < 0$) and downstream ($t > 0$). The ring waves in the upstream and the transverse waves of outer-V waves in the downstream are of same frequency and higher than the encounter frequency defined in the moving coordinate system. This is confirmed by the time-frequency spectrograms presented on the lower part of Figure 4. The spectrograms corresponding to $(X_0, Y_0) = (0, 2)$ and $(X_0, Y_0) = (0, 8)$ are illustrated on the left and right of Figure 4 (lower part), respectively. The frequency of upstream ring waves and that of downstream transverse waves are equal to $\Omega = 2\omega$ according to eq.(17) in [6]. Similar to the case of $\tau = 0.2$, there are two slanting branches of L-shaped boomerangs associated with the inner-V and outer-V waves.

The Spatial Hilbert Transform Method (SHTM) has recently been developed and summarized in [16] for multi-directional wave fields. Assuming the input waves represented by $\eta(X, Y, t)$ as a function of space (X, Y) and time t, spatial Hilbert transforms $\mathbb{H}_X$, $\mathbb{H}_Y$, $\mathbb{H}_{XY}$ at each time instant t with respect to X, Y and (X, Y) are used to obtain an envelope function $A(X, Y, t)$ and a phase function $\gamma(X, Y, t)$. Both $A(X, Y, t)$ and $\gamma(X, Y, t)$ are real functions and used to reconstruct the input waves by

$$\eta(X, Y, t) = A(X, Y, t) \cos[\gamma(X, Y, t)] \tag{27}$$

of which the phase function can be assumed to be expressed by

$$\gamma(X, Y, t) = K_1 X + K_2 Y - \Omega\, t + \gamma_0 \tag{28}$$

with an initial phase γ_0 independent of (X, Y, t). Furthermore, the local wavenumbers (K_1, K_2) and frequency Ω are assumed to be slowly-varying with respect to the space-time variables (X, Y, t) so that

$$\begin{aligned} K_1 &\approx \partial\gamma/\partial X \\ K_2 &\approx \partial\gamma/\partial Y \\ \Omega &\approx -\partial\gamma/\partial t \end{aligned} \tag{29}$$

following [18]. Once (K_1, K_2, Ω) are obtained at (X, Y, t) by using (29), the local phase $\mathbf{V}_p$ and group velocity $\mathbf{V}_q$ vectors are defined by

$$\begin{aligned} \mathbf{V}_p(X, Y, t) &= \Omega(K_1, K_2)/(K_1^2 + K_2^2) \\ \mathbf{V}_g(X, Y, t) &= (\partial\Omega/\partial K_1, \partial\Omega/\partial K_2) \end{aligned} \tag{30}$$

according to [13]. This SHTM developed in [16] is applied to analyze unsteady ship waves. As an example, the special case of $\omega = 1$ and $F_{\mathrm{r}} = 0.251$ is considered and the local phase velocity vectors $\mathbf{V}_p(X, Y, t)$ are illustrated by the red arrows in Figure 5 over the wave patterns. The pictures at the instant $t = 0$ and $t = 10$ are drawn on the upper part and lower part of the Figure, respectively. The orientation of local phase velocity is well shown to be at the right angle to crestlines. The magnitude of ring-fan waves (both upstream and downstream) is much larger than that of transverse and divergent waves which are present only downstream.

Finally, the time-harmonic ship waves around the Wigley IV hull are computed by HydroStar-V and illustrated in Figure 6 for the special case of $\tau = 0.2499$. There are 3x3 pictures on each of which the real and imaginary parts of $\phi_j(x, y, z = 0)$ for $j = 3, 5, 9, 11, 1$ and 13 associated with the boundary condition (11) on the hull, evaluated by using HydroStar-V are depicted in the upper half and lower half, respectively. On the left column, the potentials $\phi_3(n_3)$, $\phi_5(n_5)$ and $\phi_1(n_1)$ are shown at the first line, second and third line, respectively, while on the right column, $\phi_9(m_3)$, $\phi_{11}(m_5)$ and $\phi_{13}(\mathrm{dif})$ are presented. Upstream ring waves are of large amplitude and downstream V-waves are originated mostly from the bow part. Remarkable differences are shown in the close vicinity of hull although wave patterns are similar at some distance from the hull. Their TFS will be shown during the presentation at conference.

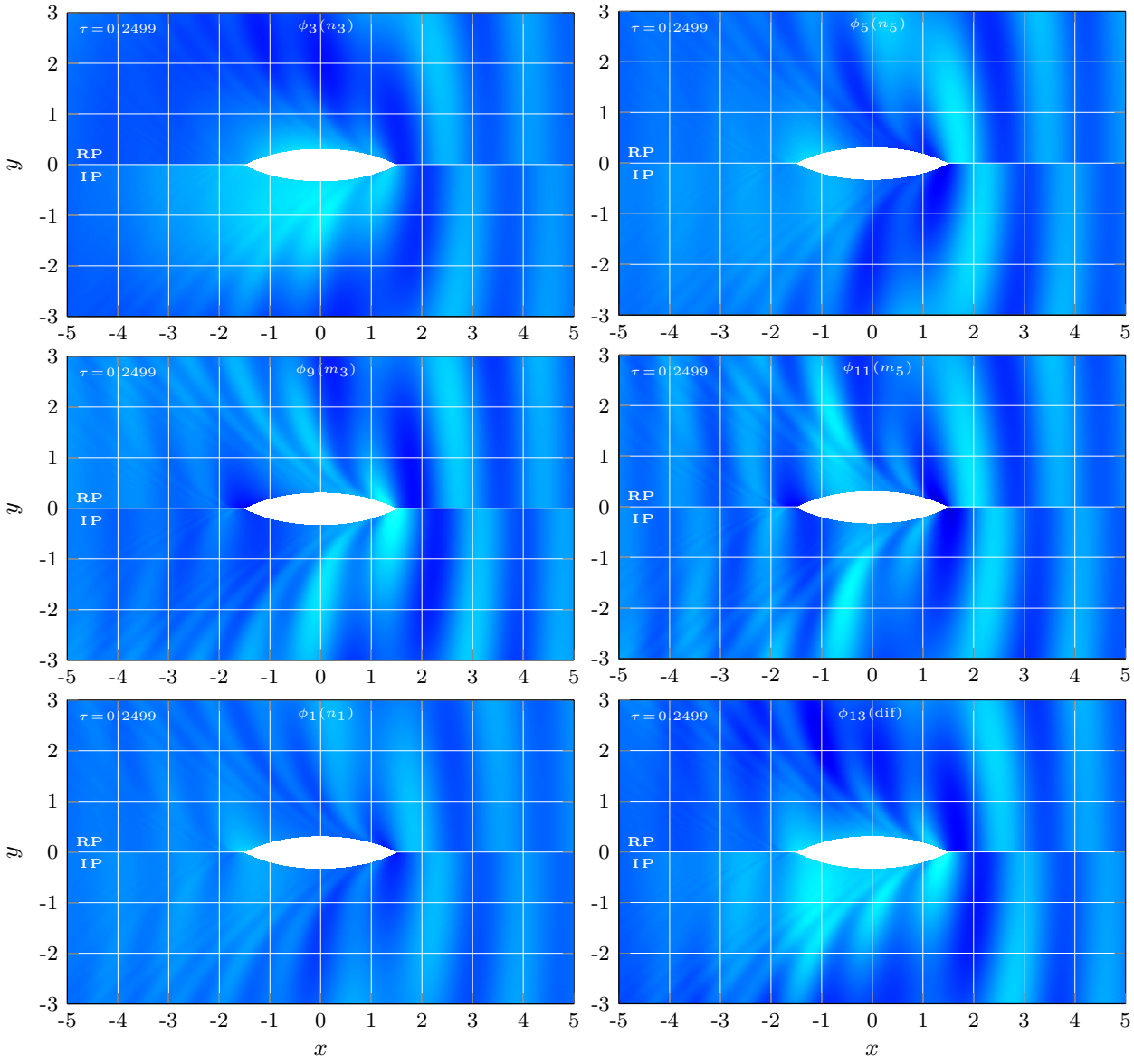

FIGURE 6 – Time-harmonic ship waves around Wigley IV hull for $\omega = 1$ and $F_{\mathrm{r}} = 0.2499$: $\phi_3(n_3)$ & $\phi_9(m_3)$ at the first line, $\phi_5(n_5)$ & $\phi_{11}(m_5)$ at the second line and $\phi_1(n_1)$ & $\phi_{13}(\mathrm{dif})$ at the third line. On each of six pictures, the real and imaginary parts are illustrated on the upper and lower halves, respectively.

IV – Conclusion

The time-harmonic ship waves, limited to the velocity potential for the sake of simplicity without loss of generality, are analyzed in both the moving and earth-fixed coordinate systems. Composed of several distinct wave systems, including ring waves, V-waves and ring-fan waves, they are of the same frequency (encounter frequency) in the moving reference system, i.e., by observation on the ship. On the contrary, ship-generated waves are of different frequencies depending on the observation location in the earth-fixed reference. Accordingly, different wave lengths and wave propagation directions are observed, depending on the location and time. By using the windowed short-time FFT and SHTM, we are able to obtain time-frequency spectrograms (TFS) and local phase-velocity vector maps. The results are insightful to better understand ship-generated time-harmonic waves. They provide not only important information of unsteady wakes, useful to detect ship speed and heading from wave field measurements, but also indications of wave breaking event through the so-called kinematic breaking threshold, i.e., the ratio of fluid velocity and phase speed.

Références

[1] M. Abramowitz and I. A. Stegun. *Handbook of Mathematical Functions : with Formulas, Graphs, and Mathematical Tables, 10th printing*. Number 55. National Bureau of Standards, 1972.

[2] X. B. Chen. Analytical features of unsteady ship waves. In *Advances in Engineering Mechanics – Reflections and Outlook*. World Scientific Publishing, 2004.

[3] X. B. Chen. Fundamental solutions to ship-motion problems with viscous effects. *Physics of Fluids*, 35(9) :097130, 09 2023.

[4] X. B. Chen, F. Dias, and W. Y. Duan. Introduction of dissipation in potential flows. In D. C. Wan, editor, *Proceeding of the 7th International Workshop on Ship Hydrodynamics, Shanghai, China*. 2011.

[5] X. B. Chen and H. Liang. Time-harmonic ship waves from the perspective of an earth-fixed observer. In *Proc. 43rd Intl Conf. Ocean, Offshore and Artic Engineering (OMAE2024-126667)*. Singapore EXPO, Singapore, 2024.

[6] X. B. Chen and H. Liang. Unsteady ship waves observed both on the ship and at sea. In *Proc. 39th International Workshop on Water Waves and Floating Bodies (IWWWFB)*, 2024.

[7] X. B. Chen, M. Q. Nguyen, I. Ten, C. Ouled Housseine, Y. M. Choi, L. Diebold, S. Malenica, G. De-Hautecloque, and Q. Derbanne. New seakeeping computations based on potentials linearised over the ship-shaped stream. In *Proceeding of the 15 Intl Symp on Practical Design of Ships and Other Floating Structures, PRADS 2022, Dubrovnik, Croatia*. 2022.

[8] X. B. Chen and G. X. Wu. On singular and highly oscillatory properties of the Green function for ship motions. *Journal of Fluid Mechanics*, 445(1) :77–91, 2001.

[9] P. Guével. L'écoulement à surface libre : Préliminaires mathématicques. *Ecole Nationale Supérieure de Mécanique (ENSM), University of Nantes, Nantes, France (in French)*, 1980.

[10] H. Liang, Y. Li, and X. B. Chen. Physical properties of the ship wake and its detection. In *Proc. 38th International Workshop on Water Waves and Floating Bodies*. Michigan, USA, 2023.

[11] H. Liang, Y. Li, and X. B. Chen. An earth-fixed observer to ship wvaes. *Journal of Fluid Mechanics*, 984(A14), 2024.

[12] H. Liang, C. Ouled Housseine, and X. B. Chen. Efficient methods free of irregular frequencies in wave and solid/porous structure interactions. *Journal of Fluid and Structures*, 98 :1–16, 2020.

[13] M. J. Lighthill. *Waves in Fluids*. Cambridge University Press, 1978.

[14] J. N. Newman. The theory of ship motions. *Advances in Applied Mechanics*, 18 :221–283, 1978.

[15] J. N. Newman. The quest for a three-dimensional theory of ship-wave interactions. *Philosophical Transactions of the Royal Society A : Math. Phys. and Engineering Sciences*, 334(1634) :213–227, 1991.

[16] Y. Wang and G. Ducrozet. Evaluating instantaneous crest phase speed in multi-directional seas through Hilbert transform. In *Proc. 39th International Workshop on Water Waves and Floating Bodies*, 2024.

[17] W. T. Waskito, M. Kashiwagi, H. Iwashita, and M. Hinatsu. Prediction of nonlinear vertical bending moment using measured pressure distribution on ship hull. *Applied Ocean Research*, 101, 2020.

[18] G. B. Whitham. Group velocity and energy propagation for three-dimensional waves. *Communications on Pure and Applied Mathematics*, 14(3) :675–691, 1961.